Available online at www.sciencedirect.com
SCIENCE DIRECT
Geochimica et Cosmochimica Acta 70 (2006) 3677–3688
Geochimica
www.elsevier.com/locate/gca

In situ iron isotope ratio determination using UV-femtosecond laser ablation with application to hydrothermal ore formation processes

Ingo Horn [a,*], Friedhelm von Blanckenburg [a], Ronny Schoenberg [a], Grit Steinhoefel [a], Gregor Markl [b]

[a] Universität Hannover, Institut für Mineralogie, Callinstr. 3, D-30167 Hannover, Germany
[b] Universität Tuebingen, Institut für Geowissenschaften, Wilhelmstr. 56, D-72074 Tüebingen, Germany

Received 28 November 2005; accepted in revised form 2 May 2006

Abstract

The feasibility of in situ stable Fe isotope ratio measurements using UV-femtosecond laser ablation connected to a multiple-collector inductively coupled plasma mass spectrometer (MC-ICP-MS) has been investigated. Different types of matrices, independently determined by solution MC-ICP-MS after chromatographic separation of Fe, have been analysed by laser ablation using the isotopically certified iron reference material IRMM-014 as the bracketing standard. The samples have been pure iron metal (JM Puratronic), Fe-meteorites (North Chile, Glenormiston and Toluca), the meteorite phases kamacite and taenite in Toluca and Fe-sulphides. Furthermore, Fe isotope ratios from hydrothermal hematite, siderite and goethite from an old mining area in the Schwarzwald, Germany, and of magnetite from the metamorphic Biwabik iron formation have been determined. The results show that a precision of better than 0.1‰ (2 sigma) can be achieved with laser ablation and that all the results obtained agree with those determined by solution ICP to better than 0.1‰. This precision and accuracy is achievable in both raster and spot ablation mode. A matrix-matched bracketing standard is not required , and all these materials can be measured accurately against a metal standard. The hydrothermal minerals show significant Fe isotope zonations. In some samples the range of δ^{56}Fe in a single aggregate encompasses the entire spectrum of ratios found by bulk solution analyses in multiple samples distributed over the whole mining district. For example, isotopic zonations found in secondary fibrous hematites show a continuous change in the δ^{56}Fe values from −0.5‰ in the core to −1.8‰ in the rim. Primary hydrothermal siderite shows the reverse pattern with lighter values in the core than in the rim. While the siderite is thought to record primary fluid histories, the hematite pattern is interpreted as a reworked isotopic signature generated by oxic dissolution of primary zoned siderite and immediate close range re-precipitation of the oxidized Fe. Abrupt changes are documented for secondary goethite showing a distinct overgrowth that is 0.4‰ lighter than the core of the grain. If indeed Fe isotopes in secondary minerals from hydrothermal ore deposits record the initial isotopic signatures of their precursor minerals, and these in turn record hydrothermal fluid histories, then the tools are in place for a detailed reconstruction of the deposit's genesis. We expect similar observations from other Fe-rich deposits formed at intermediate and low-temperatures (e.g. banded iron formations). Laser ablation now provides us with the spatial resolution that adds a further dimension to our interpretation of stable Fe-isotope fractionation.

1. Introduction

An increasing interest in processes generating mass-dependent isotope fractionation of Fe in natural environments is documented by the variety of publications in the last 2 years. Many of these investigations are experimental and address the fundamental mechanisms of Fe-isotope fractionation by inorganic and biotic processes (Matthews et al., 2001; Skulan et al., 2002; Welch et al., 2003; Brantley et al., 2004; Croal et al., 2004; Icopini et al., 2004; Johnson et al., 2004, 2005; Wiesli et al., 2004; Anbar et al., 2005; Butler et al., 2005; Poulson et al., 2005; Walczyk and von Blanckenburg, 2005), while others focus on the observed variations in natural settings throughout the Earth's

* Corresponding author.
E-mail address: i.horn@mineralogie.uni-hannover.de (I. Horn).

0016-7037/$ - see front matter © 2006 Elsevier Inc. All rights reserved.
doi:10.1016/j.gca.2006.05.002

history (Zhu et al., 2001; Kehm et al., 2003; Anbar, 2004; Beard and Johnson, 2004b; Dauphas et al., 2004; Fantle and De Paolo, 2004; Matthews et al., 2004; Poitrasson et al., 2004, 2005; Rouxel et al., 2004, 2005; Severmann et al., 2004; Williams et al., 2004; Weyer et al., 2005; Dauphas and Rouxel, 2006; Markl et al., 2006). All of these studies have been carried out using solution nebulization multi-collector inductively coupled plasma mass spectrometry (MC-ICP-MS) after sample dissolution and chemical purification using chromatography.

The in situ determination of stable Fe isotopes by laser ablation (LA) coupled to multiple-collector ICP-MS is a relative recent development. This delay is in part due to the small variations observed in nature, which are approximately 4‰ in the $^{56}Fe/^{54}Fe$ ratio (Anbar, 2004; Beard and Johnson, 2004a). Therefore, in order to study the fractionation of Fe isotopes in natural processes the precision with either solution or by laser ablation sample introduction needs to be about 0.2‰ or better.

Laser ablation ICP-MS has the potential to resolve in situ variations in the stable metal isotopes on the micrometer scale. This technique has so far been successfully applied to the determinations of trace element concentrations in a large variety of matrices and is widely used for U/Pb geochronology of zircons and other minerals (Horn et al., 1997, 2000; Günther et al., 1998, 2001; Mason and Mank, 2001; Russo et al., 2002; Eggins, 2003). With the increasing use of MC-ICP-MS systems, laser ablation has provided highly precise data on a number of radiogenic isotope systems. Successful applications cover Sr, Hf, and Pb isotope ratio measurements (Thirlwall and Walder, 1995; Ramos et al., 2004; Woodhead et al., 2004, 2005; Halpin et al., 2005). These systems provide an advantage in that the instrumental mass discrimination, amounting to a few percent in MC-ICP-MS, can be corrected using a stable reference ratio (e.g. Tl for Pb).

Heavy stable isotope ratios are a new challenge for in situ studies. Percent level concentrations are required for isotope ratio determinations of sufficient precision to resolve the small isotopic ratio shifts expected for stable metals. To date, this technique has been applied mainly to Mg isotopes (Young et al., 2002), and initial studies to measure iron isotopes have been made by Graham et al. (2004) and Kosler et al. (2005). However, a major obstacle arises from the fractionation of elemental or isotopic ratios during ablation and analysis as seen in traditionally employed nanosecond Nd:YAG or Excimer laser systems which is in direct relation to the process of thermal ablation generated by the interaction of nanosecond laser pulses with the sample (Horn et al., 2006). This fractionation makes it difficult to achieve the precision needed for today's applications.

An additional drawback for laser ablation analysis is the lack of solid, isotopically certified reference materials that are homogeneous at the micron scale and available for the type of phases (minerals) under investigation. The commonly employed nanosecond laser ablation systems require a standard that consists of a similar matrix to the material under investigation.

All laboratories investigating the potential of LA-MC-ICP-MS to determine metal isotope fractionation use nanosecond pulse width laser ablation systems operating in the ultraviolet (UV) together with a matrix-matched calibration standard (Graham et al., 2004). These types of laser ablation systems have been investigated for their suitability in the determination of heavy stable isotope ratios of Fe and Cu. However, it was found that a substantial change in isotopic fractionation exceeding several ‰ in $\delta^{56}Fe$ is produced during the process of laser ablation when performing a spot analysis (Kosler et al., 2005). Similar results have been found for the Cu isotope system where a 1.8–4.8‰ change in the $\delta^{65}Cu$ has been observed (Jackson and Guenther, 2003). Both investigations relate this "laser ablation-induced" isotope fractionation to a particle-related phenomenon, produced through incomplete vaporisation and ionisation of the ablated aerosol in the ICP at temperature above 4000 K. Theory predicts that there should be negligible fractionation at these temperatures (Schauble, 2004). We suggest that these isotope ratio shifts are introduced by irregular and irreproducible ablation conditions, such as thermally induced effects (melting, recondensation) and particle size effects that propagate into shifts in the mass spectrometers mass bias (Horn et al., 2006).

In order to overcome the problems known from nanosecond laser ablation, we employed a frequency-quadrupled femtosecond laser operating at a wavelength of 196 nm. Femtosecond laser pulses moves the ablation process away from thermal ablation, which provides significant advantages in terms of particle size, matrix dependency, transport efficiency, and stability. It has been demonstrated that the use of UV (266 nm) femtosecond pulses for ablation eliminates elemental fractionation, which is a severe limitation when trying to determine the Pb/U ratios (Poitrasson et al., 2003). Here, we demonstrate the precision and accuracy of stable iron isotope ratio determinations using this new technique. We then proceed to apply this new system to trace hydrothermal ore petrogenesis on the micrometer scale.

2. Methods

In order to investigate the feasibility of heavy stable isotope ratio measurements using laser ablation, a proof of accuracy and precision has to be carried out. Ideally, this should involve several types of matrices with known isotopic composition. However, the only certified and available reference material is the IRMM-014, a pure Fe-metal that is almost exclusively used as the bracketing standard for Fe-isotope analysis. Most solution ICP-MS studies report $\delta^{56}Fe$ values with respect to IRMM-014 (Belshaw et al., 2000; Kehm et al., 2003; Weyer and Schwieters, 2003; Schoenberg and von Blanckenburg, 2005).

In this study, we calibrated a variety of different matrices, such as pure iron (Johnson Matthey, puratronic, lot No. FE495007IF2, 99.995% Fe), iron meteorites, goethite, hematite, magnetite, and siderite by solution ICP-MS after chemical purification employing the standard—sample—bracketing technique as described by Schoenberg and von Blanckenburg (2005) (Table 1). All analyses have been carried out on a Thermo Finnigan Neptune multi-collector ICP-MS in our laboratory in Hannover. The long-term reproducibility of our solution measurements yields a δ^{56}Fe value of better than ±0.05‰ (2 sigma). All Fe-isotopic measurements (solution ICP and laser ablation) are reported as δ^{56}Fe, defined by:

$$\delta^{56}\mathrm{Fe}_{\mathrm{IRMM-14}} = \left[\frac{(^{56}\mathrm{Fe}/^{54}\mathrm{Fe})_{\mathrm{Sample}}}{(^{56}\mathrm{Fe}/^{54}\mathrm{Fe})_{\mathrm{IRMM-14}}} - 1\right] * 1000.$$

The measurements, both for solution and for laser ablation, are carried out in high mass resolution ($\Delta m/m = 9000$–$10{,}000$ as defined Weyer and Schwieters (2003)) in order to resolve the spectral interferences of argon nitrites and argon oxides on ^{54}Fe, ^{56}Fe, ^{57}Fe, and ^{58}Fe. The detector array of Faraday cups is set to acquire the ion beams of ^{52}Cr, ^{54}Fe, ^{56}Fe, ^{57}Fe, ^{58}Fe, and ^{60}Ni. Cr and Ni are monitored and used for correction of the isobaric interferences on ^{54}Fe and ^{58}Fe.

2.1. 196 nm femtosecond laser ablation

Our in-house built laser ablation system is based on a 100 femtosecond (fs) Ti-sapphire regenerative amplifier system (Hurricane I, Spectra Physics, USA) operating at a fundamental wavelength of 785 nm in the infrared spectra (IR). Subsequent harmonic generations produce the wavelengths 393 nm in the second, 262 nm in the third and 196 nm in the fourth stage. The pulse energies, measured with a pyroelectric sensor (Molectron, USA), are 1.0 mJ/pulse at 785 nm, 0.25 mJ/pulse at 262 nm, and 0.03 mJ/pulse at 196 nm. After the fourth harmonic generation stage, the 196 nm beam is steered by four dichroic mirrors into a 10× objective (OFR, USA) and focussed onto the sample. Spot size can be adjusted by means of a variable and motorized iris mounted at a distance of 2 m from the objective. At this distance, a demagnification ratio of 100 is reached resulting in a maximum achievable spot diameter of 35 μm. Within this spot, an energy density of 1.5 J/cm^2 can be maintained, sufficient to ablate silicates. The layout of the system is illustrated schematically in Fig. 1.

The pulse width has been determined after the frequency conversion using autocorrelation of the unconverted IR beam, which did not show any degradation from the initial pulse width of 100 fs. However, a direct measurement of the pulse width in the UV range cannot yet be performed. Therefore, it has to be assumed that the pulse width in the UV may be doubled to ~200 fs by the optical elements introduced. The visualisation uses a CCD camera and zoom objective either in transmitted or reflected light mode. A motorized stage with software control (from a modified New Wave LUV266 system) enables fast spot location changes for the standard sample bracketing technique and allows rasters to be produced over larger areas to extend the ablation signal time and to ensure signal height stability. This allows a signal intensity match similar to the procedure described in Schoenberg and von Blanckenburg (2005). The ablation cell, made from aluminium, has an active volume of 30 cm^3, which is flushed with helium or argon through three inlets. The samples are mounted using an insert allowing either a thin section together with two 12.5 mm standard blocks or three 25 mm sections to be mounted flush with the insert top. When using helium as the aerosol carrier gas, an additional make-up flow of argon is added just before entering the torch of the ICP. A gas flow of ca. 1 L/min helium together with 0.8 L/min argon has been used for the experiments. Tuning conditions of the ICP-MS were similar to those used during solution nebulization Schoenberg and von Blanckenburg, 2005 with the exception of the extraction potential, which was set from −2000 to −1300 V when using helium.

Table 1
fs-LA-MC-ICP-MS and reference data (solution MC-ICP-MS) for the analysed samples (all values in ‰)

Sample	Material	δ^{56}Fe Laser ablation	2 SD	δ^{56}Fe solution	2 SD	Reference
JM Puratronic	Fe-metal	0.06	0.06	0.09	0.05	Schoenberg (unpublished)
Glennormiston	Fe-meteorite	0.03	0.13	0.03	0.05	Schoenberg (unpublished)
North Chile	Fe-meteorite	0.06	0.07	0.03	0.05	This work
				0.05	0.11	Poitrasson et al. (2005)
Toluca	Fe-meteorite	−0.06	0.06	0.07	0.06	Schoenberg (unpublished)
				0.04	0.06	Zhu et al. (2001)
	Kamacite	−0.06	0.06			
	Taenite	0.14–0.34		0.24	0.09	Poitrasson et al. (2005)
M420	Siderite	−0.91*	0.11*	−0.85	0.05	Markl et al. (2006)
Fe13	Hematite	−1.27*	0.06*	−1.16	0.05	Markl et al. (2006)
PHB4	Hematite	−0.58		−0.58	0.05	Core: Markl et al. (2006)
		−1.3 to −1.8		−1.50	0.05	Rim: Markl et al. (2006)
QFS26	Goethite	−0.48*	0.07*	−0.51	0.07	Markl et al. (2006)

* Robust median (Isoplot by Ludwig, 2001) for inhomogeneous samples, 2SD: 2σ external reproducibiliy (with exception for *, robust median).

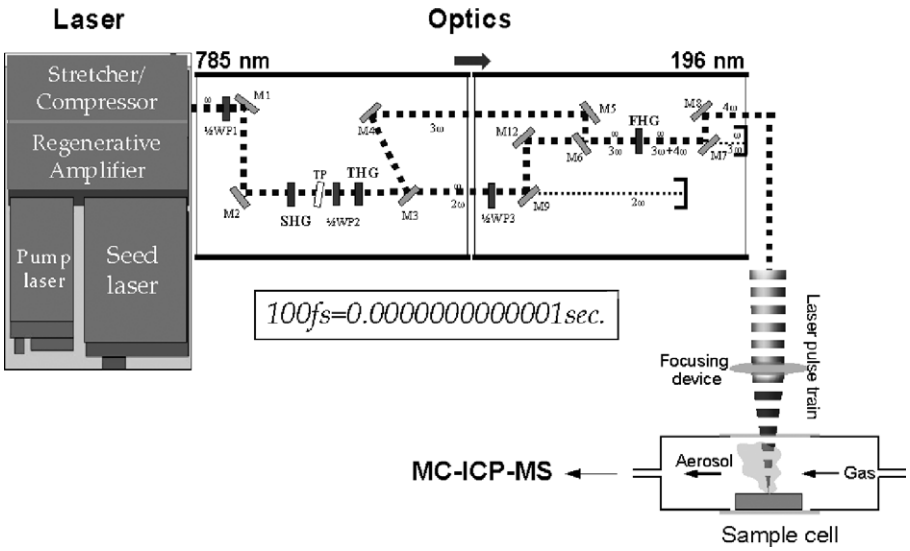

Fig. 1. Schematic diagram of the 196 nm femtosecond laser ablation system illustrating the wavelength conversion set-up from IR to deep UV (WP, wave plate; M, mirror; SHG, second harmonic generator; THG, third harmonic generator; FHG, fourth harmonic generator; ω, frequency).

2.2. Acquisition parameters

The acquisition parameters for the raster and spot analyses, performed in static mode on faraday cups, were set to acquire 60–100 cycles of 2 s integrations each. The spot size was kept at 35 μm, regardless of ablation mode used. On-peak-zero measurements were not subtracted since the observed background signal on mass ^{56}Fe was less than 0.2 mV, measured on a 10^{11} Ohm resistor. After a warm-up period of the ICP-MS, measurements of an Fe-metal sample were performed until the drift of the instrument, with respect to mass stability, was less than 100 ppm over a period of 8 min, which covers the time interval for a standard-sample-standard measuring sequence. The analyses were performed using identical beam sizes for the raster and the spot analyses. Repetition rates of 5–10 Hz have been employed giving a signal intensity of up to 50 V for a pure iron sample. Oxides or carbonates contain less Fe than the pure metal used as bracketing standard, and, therefore usually produced lower Fe ion beams. Since equal Fe beams for both standard and sample are a requirement of the bracketing technique if no background subtraction is carried out, the repetition rates for sample analyses were increased accordingly.

In order to evaluate the data quality with respect to potential interferences from molecular species and isobaric overlaps of Cr, samples from each analytical session were plotted on a three-isotope plot together with the theoretical mass fractionation line using δ^{56}Fe versus δ^{57}Fe. There are no processes identified so far that yield mass-independent of Fe-isotopes fractionation, thus all data are expected to plot on the theoretical mass-dependent fractionation line. Potentially, uncorrected isobaric or molecular overlaps on ^{54}Fe would result in a shift away from the theoretical fractionation line. For example, a signal intensity of 4×10^{-13} A on ^{52}Cr and 1.9×10^{-10} A on ^{56}Fe, assuming an error of 5% for the Cr correction on mass 54, would result in an error on δ^{56}Fe of 0.045‰. However, all analysed samples had ^{52}Cr intensities of less than 1×10^{-15} A. Individual errors of the analyses have been calculated by propagating the analytical errors of the bracketing standard with those of the samples. All acquired data lie within their 2-sigma uncertainties on the fractionation line, regardless of the matrix analysed (e.g. Fig. 2).

3. Results

3.1. Matrix-matched samples (pure Fe-metal)

Since the available solid IRMM-14 metal blocks are small and would require frequent re-polishing when used as bracketing calibration standard during laser ablation, a secondary metal standard (Fe 99.995%, Puratronic, Johnson Matthey, lot No. FE495007IF2) has been calibrated using both solution ICP-MS and laser ablation. The calibration was performed on ablation rasters of 150×150 μm on both standard and sample. Since both are composed of pure Fe, this experiment represents ideal conditions with respect to a matrix match of standard and sample. The δ^{56}Fe value with respect to IRMM-14 obtained in solution is 0.09 ± 0.05‰, which agrees well with the δ^{56}Fe of $0.06‰\pm0.07$ (2 sigma) determined using UV-femtosecond laser ablation. All acquired data plot within analytical error (2 sigma) on the mass-dependent fractionation line shown in Fig. 2A.

3.2. Iron meteorites and their main phases kamacite and taenite

The second set of samples are the iron meteorites North Chile, Glenormiston and Toluca. Iron meteorites are different to the pure metal samples used as bracketing standards

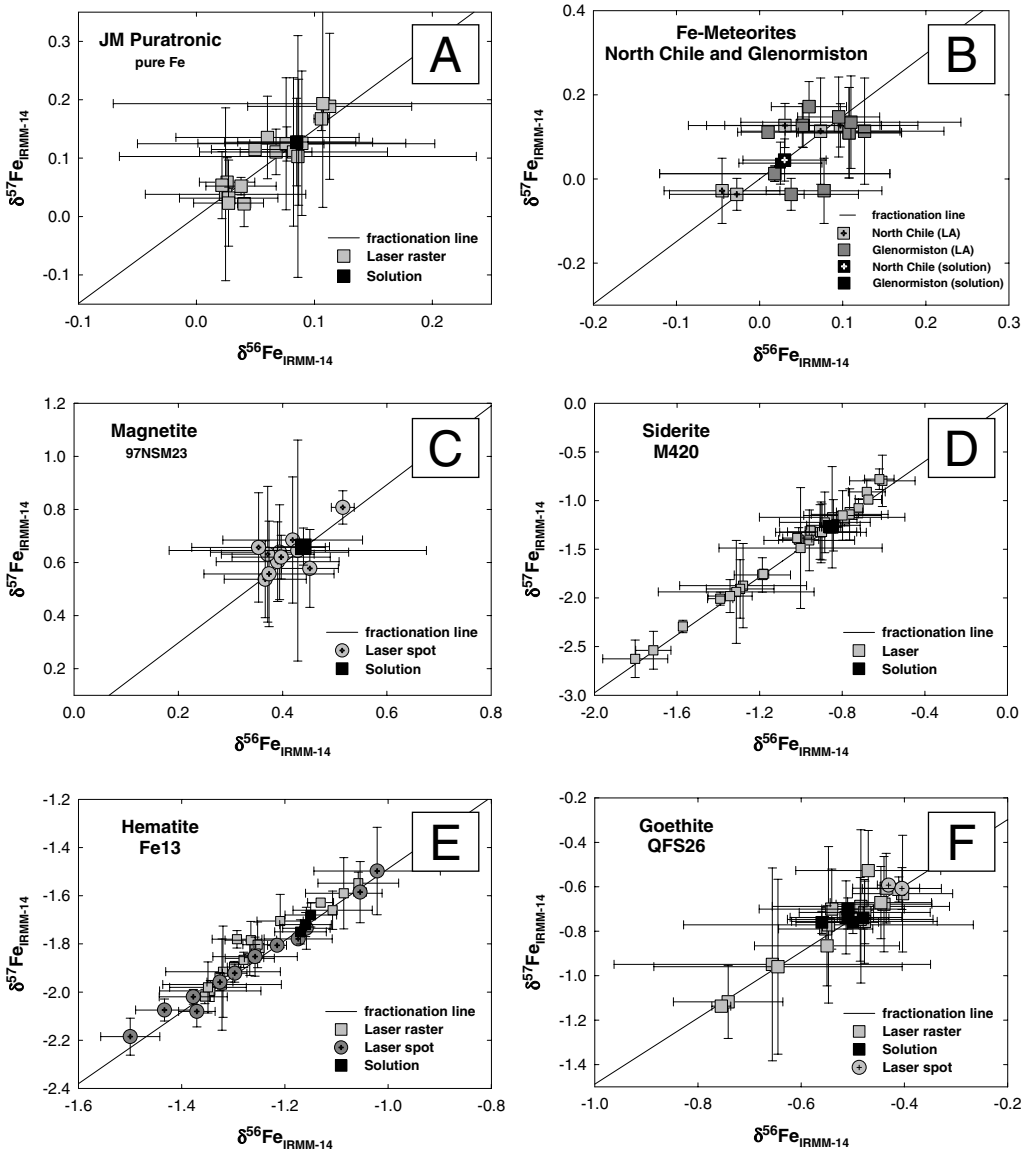

Fig. 2. Three-isotope plots for the analysed samples illustrating that no interferences influence the measurement undertaken using laser ablation MC-ICPMS. (A) Measurements of the secondary standard JM Puratronic in comparison to solution MC-ICP-MS results from our laboratory. (B) Laser ablation measurements of the iron meteorites North Chile and Glenormiston in comparison to conventional solution MC-ICP-MS results measured in our laboratory. Note that Poitrasson et al. determined the δ^{56}Fe value of North Chile with $0.05 \pm 0.11‰$ (not shown). (C) Results from the analysis of high-temperature metamorphic magnetite showing the precision obtainable by UV-femtosecond laser ablation when using a spot size of 35 μm. The results obtained are in perfect agreement with solution analysis of mineral separates obtained after chromatographic separation of Fe and solution ICP (Frost et al., 2005). (D) Analysis of hydrothermal siderite from the Sophia mine, Schwarzwald, Germany, showing a discontinuous array of values. The average δ^{56}Fe value of $-0.838‰$ (LA, 27 analyses) agrees well with the δ^{56}Fe value of $-0.85‰$ (3 analyses) determined by solution ICP when representative sampling of the whole grain is carried out. (E) Analyses of secondary hydrothermal hematite Fe13 from Streckfeld, Wolfach, Schwarzwald, Germany, shows a large range of δ^{56}Fe values illustrating that low-temperature hydrothermal processes can generate large isotope variations. The spot analyses carried out with a diameter of 35 μm fully agree with the raster analyses illustrating that no differences are observed when using the raster or spot mode for laser ablation. (F) Fe-isotope analyses of a hydrothermal goethite grain from the Dorothea mine, Schwarzwald, Germany, show a discontinuous range of δ^{56}Fe values. Seventeen analyses cluster around $0.48‰$ while only four analyses show up to $0.4‰$ higher values, which corresponds to the observed abrupt changes shown in Fig. 8. The spot analyses illustrate that no differences are found between raster and spot analyses when UV-femtosecond laser ablation is used.

in that they contain significant and variable concentrations of Ni (5–16 wt%) and high concentrations of Co (0.4–0.7 wt%) (Rasmussen et al., 1984). The other transition metals such as the possible interferent Cr show much lower concentrations, ranging from 18 to 240 μg/g (Choi et al., 1995). The variable Ni concentrations occur mainly due to variable amounts of taenite, an Fe–Ni alloy containing up to 21 wt% Ni, while the groundmass composed of kamacite contains ~7 wt% Ni (Choi et al., 1995; Rasmussen et al., 1988). Significant amounts of C and S can be attributed to the occurrence of coenite, a Fe-carbide, or troilite, a Fe-sulphide.

Some groups have now investigated the iron isotopic composition of iron meteorites using solution nebulization which nearly exclusively show δ^{56}Fe values in a vary narrow range for bulk iron meteorites of −0.02 to 0.13‰ with respect to IRMM-14 (Zhu et al., 2002; Kehm et al., 2003; Beard and Johnson, 2004a; Poitrasson et al., 2004, 2005). Our solution ICP measurements yield a δ^{56}Fe of 0.03 ± 0.05‰ for North Chile and 0.03 ± 0.05‰ for Glenormiston (Schoenberg, unpublished). This lies well within the published range of iron meteorite results (Fig. 2B). Poitrasson et al. (2005) determined δ^{56}Fe of North Chile by solution ICP to be 0.05 ± 0.11‰.

The laser ablation analyses agree well with the published data, yielding a δ^{56}Fe of 0.03 ± 0.13‰ for North Chile and 0.06 ± 0.07‰ for Glenormiston (Fig. 2B). It is important to note that the variability between the analyses in Fig. 2B is much larger than the internal uncertainty of the measurements. As will be shown below, we attribute this to sample heterogeneity and not to a mass bias artefact.

Conventional Fe-isotope determinations obtained by micro drilling from kamacite and taenite in the iron meteorites Toluca and Cranbourne by Poitrasson et al. (2005) show significant differences in their δ^{56}Fe values, with taenite being consistently 0.1–0.3‰ heavier than kamacite. The laser ablation results confirm the difference and the absolute δ^{56}Fe value for taenite is ~0.24‰ heavier than IRMM-014 (Figs. 3 and 4). Note that taenite results showed a larger variability than those of kamacite, which could be due to the fact that kamacite matrix was "tapped" while deepening the laser crater into the small taenite grain. Another possibility is that during cooling of the meteorite parent body, a disequilibrium effect or diffusion-caused zonation known especially for Co and Ni in taenite (Rasmussen et al., 1988) also produces an Fe-isotopic zonation. The individual analyses of taenite also had a reduced precision due to a relatively short acquisition time, and again the possibility that kamacite was ablated. Conventional measurements of Toluca in our laboratory yield a δ^{56}Fe of -0.07 ± 0.05‰, which agrees well with the value of

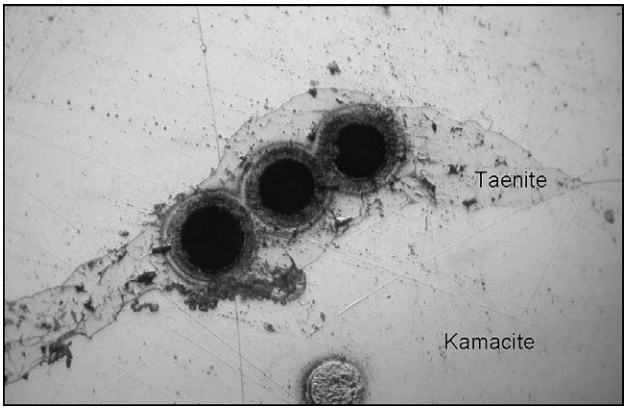

Fig. 3. Photomicrograph of the iron meteorite Toluca showing a taenite lamella with laser ablation craters having a diameter of 35 μm.

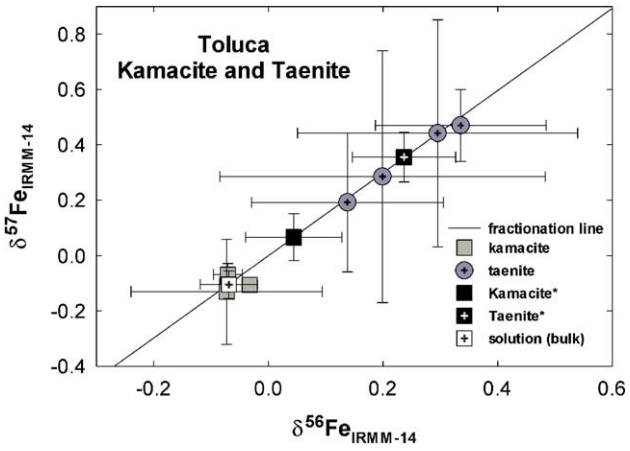

Fig. 4. Laser ablation measurements of taenite (spots) and kamacite (rasters) of the iron meteorite Toluca in comparison to solution MC-ICP-MS results measured in our laboratory (Schoenberg unpublished). Also shown are results of mechanically micro-drilled solution data of taenite and kamacite (*black symbols) separates from Poitrasson et al. (2005).

kamacite determined by laser ablation with δ^{56}Fe of -0.06 ± 0.06‰. It is 0.1‰ lower than the value determined by Zhu et al. (2001) (Fig. 4). Since both aliquots (solution/laser) determined in our laboratory come from the same small peace of Toluca, it is possible that small-scale variations in Toluca might be present. In any case, differences in the iron isotope composition might be real and can in part be due to the variable amount of taenite analysed during bulk sampling of the meteorite.

3.3. Magnetite (97NSM23)

As shown above, a change in matrix composition with respect to large concentrations of Ni and minor concentrations of Co does not affect the quality of the results obtainable by laser ablation when analyzing metals. In order to evaluate this technique further we analysed magnetite from the high-temperature metamorphic Biwabik iron formation (Minnesota, USA) that had been determined by solution ICP-MS giving a δ^{56}Fe value of 0.44‰ (Frost et al., 2005). The mineral assemblage is hedenbergite-magnetite-quartz with minor amounts of calcite. The sample has been contact metamorphosed at approximately 400 °C. The thin section used had magnetite with diameters mostly below 100 μm allowing only spot analysis to be carried out. The measurements obtained from 11 spot analysis yield a δ^{56}Fe of 0.41 ± 0.09‰ which agrees well with the conventional analysis and illustrates that a precision of better than 0.1‰ (2 sigma) can be obtained using femtosecond laser ablation (Fig. 2C).

3.4. Hydrothermal hematite, goethite and siderite from the Schwarzwald, Germany

In the absence of a suitable certified matrix standard, the iron oxide, oxy-hydroxide and carbonate analyses were bracketed against the IRMM-14 metal. A testable prere-

quisite is that differences between the matrix of the ablated materials and the standard have no significant influence on the results obtained.

The old mining area in the Schwarzwald (SW Germany) contains mineralisations formed during discontinuous hydrothermal activities over a time period of almost 300 Ma (Schwinn and Markl, 2005; Schwinn et al., 2006; Markl et al., 2006). Several samples from various barite–fluorite-quartz vein deposits have been investigated by solution ICP (Markl et al., 2006). These samples experienced two different mineralisation stages related to different fluid events: an initial, high-salinity fluid leached iron from the basement rocks and deposited it at temperatures between 120 and 250 °C as primary hematite or siderite, depending on the f_{CO2} and f_{O2} in the fluid (Brockamp and Clauer, 2005; Schwinn and Markl, 2005; Schwinn et al., 2006; Markl et al., 2006). A later fluid phase consisting, more or less, of meteoric water reacted with these primary mineralisations at temperatures below 50 °C, leached, partly oxidized and redeposited the iron as fibrous goethite or hematite. Both primary and secondary minerals were analysed by solution ICP-MS in the study of Markl et al. (2006), and some of the same samples (again covering all types of mineralisations) were analysed by laser ablation in this study.

Dark brown siderite (M420, mine Sophia) shows an average δ^{56}Fe value of −0.84‰ (LA, 27 analyses), which compares well to the δ^{56}Fe value of −0.85‰ (3 analyses) determined by solution ICP. However, the analysed grain shows a large variation in the δ^{56}Fe values across the grain ranging from −0.6 to −1.8‰. At least 3 isotopically different zones can be identified which are characterized by discontinuous δ^{56}Fe values of −1.8, −1.3 and −0.8 to −0.6‰ (Fig. 2D). The absence of intermediate values between these clearly defined zones indicates the involvement of separate mineralisation events or different precipitation mechanisms. Obviously, bulk sampling and analysis by the solution method will result in an average value that disguises much of the isotopic zonation and thereby much of the information on leaching and precipitation processes during hydrothermal and low-temperature iron mobilisation.

To confirm that the intra-crystal isotope variations are indeed a genuine feature rather than analytical artefacts, we analysed a second siderite crystal from a different sample location along a section from its core to its rim. The 6 mm large siderite grain, OCR468, from the Clara mine near Wolfach shows a macroscopic concentric zonation which corresponds to an evolution from a light Fe-isotopic signature of −1.1‰ in the core to heavier values of −0.46‰ at the rim (Fig. 5). Furthermore, the iron isotope profile also allows the identification of a later alteration event along a crack, which is superimposed on the grain as a secondary 500 μm wide overprint. This zone of alteration is clearly identifiable by its light Fe-isotopic signature (Fig. 5). However, the continuous trend to heavier values towards the rim dominates.

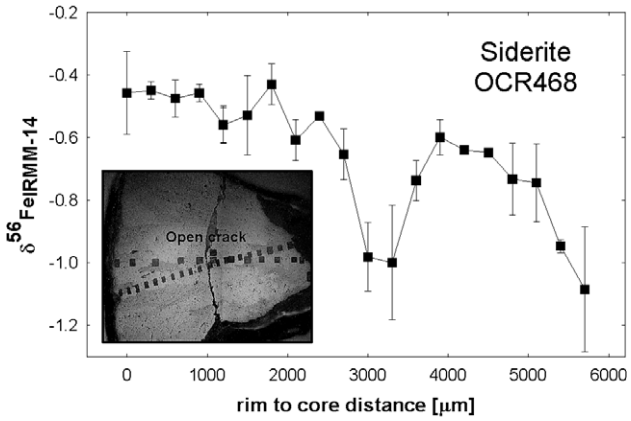

Fig. 5. Fe-isotopic profile through a concentric zoned siderite section (OCR468, mine Clara, Schwarzwald, Germany), illustrating an evolution from light Fe values towards heavier values during time of crystallisation. The data point locations correspond to the laser ablation rasters on the inlet figure. Like siderite M420, the analyses of siderite OCR468 show a large range in their δ^{56}Fe values. Note the crack in the inset and its influence on Fe-isotope composition.

For comparison, we analysed fibrous, botryoidal hematite (“Glaskopf”) from similar mineralisations in the same locality. Sample Fe13 from Streckfeld near Wolfach is composed of layers of red, feathery crystals crystallized on goethite. The growth direction for this sample could unfortunately not be identified so that no profile can be plotted for this sample. Solution ICP yielded a δ^{56}Fe value of −1.16‰ (3 analyses) while the laser ablation data from raster analyses gave an average value of −1.27‰ (robust median), with a range from −1.0 to −1.5‰ (Fig. 2E). We tested both spot and raster analyses, which were calibrated by bracketing against a raster analysis of the standard metal (IRMM-014). The average of 11 spot analyses (δ^{56}Fe = −1.27‰) agrees with the raster analyses within 0.1‰ which illustrates that the results do not depend on ablation conditions using fs-UV laser ablation. This is in contrast to the results of Kosler et al. (2005) who used a nanosecond laser ablation system.

A second fibrous hematite sample (PHB4) was analysed from the Hohberg mine near St. Roman, which is about 10 km from both the sample location for Fe13 and each of the siderite samples mentioned above. If isotopically similar, this could be interpreted in general as an underlying mechanism governing the formation and zonation of the fibrous hematite aggregates. We analysed a profile through this 2.5 cm thick fibrous radial hematite which was cut parallel to its growth direction. Trace element analyses using LA-ICP-OES (Varian Vista Pro) showed that there are no chemical gradients with respect to the elements Na, Ca, Mg, Ba, Sr, Ti, Mn, and Ni within this sample. The detected concentration for Na are below 200 μg/g while Ca, Ba, and Co are at levels of 400 μg/g and Mn shows concentrations around 700 μg/g. All other elements analysed are below 100 μg/g. Solution analysis from the core and rim of this sample show δ^{56}Fe values of −0.58 and −1.5‰, respectively (Markl et al., 2006). The laser ablation

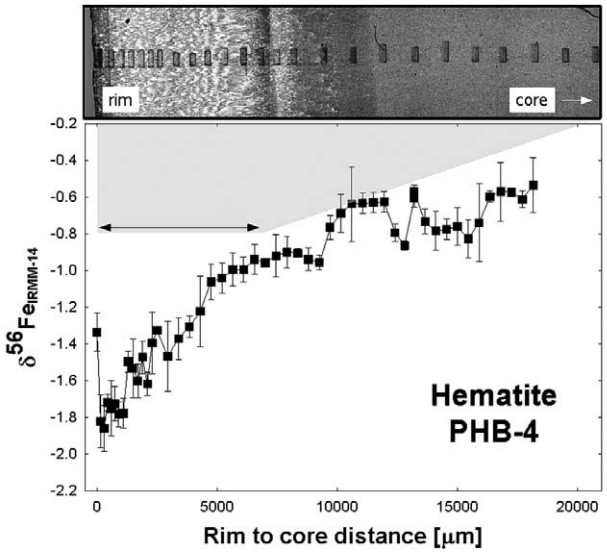

Fig. 6. δ^{56}Fe profile from rim to core of a hydrothermal hematite PHB-4 from the Hohberg, St. Roman, Schwarzwald, Germany. The data illustrate the complex hydrothermal processes during its generation, featuring abrupt and continuous changes in the isotopic signature in a 2 cm long mineral section.

analyses revealed several distinct areas, some of which being identifiable under the optical microscope. As Fig. 6 illustrates the core has a δ^{56}Fe value of −0.53‰ followed by a decrease to values of approximately −1.0‰ from where it remains constant over a distance of approx. 3 mm (Fig. 6). This zone is followed by a third decrease towards a δ^{56}Fe value of −1.5‰ and an abrupt decrease to values of approximately −1.8‰. The outermost rim of the section (outermost 200 μm), however, has a δ^{56}Fe of −1.3‰.

Hydrothermal fibrous goethite (QFS26) from the Dorothea mine near Freudenstadt yields an average δ^{56}Fe of

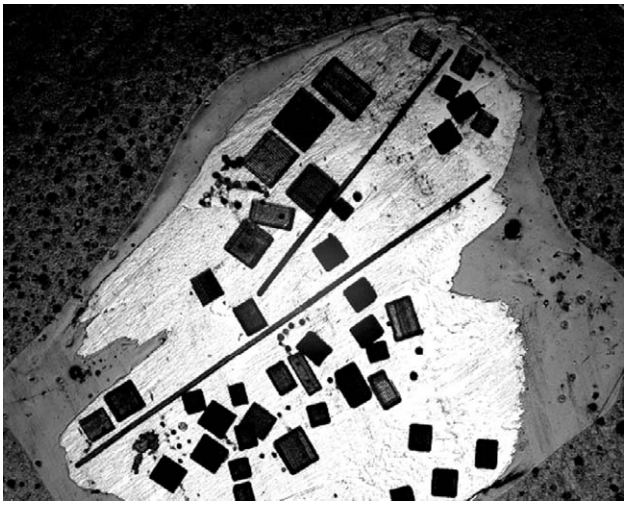

Fig. 7. Photomicrograph of the hydrothermal goethite grain QFS 26 (Fig. 7) analysed by laser ablation. The line at the top corresponds to the isotope ratio scan shown in Fig. 8. The maximum raster size corresponds to an area of 200 × 200 μm.

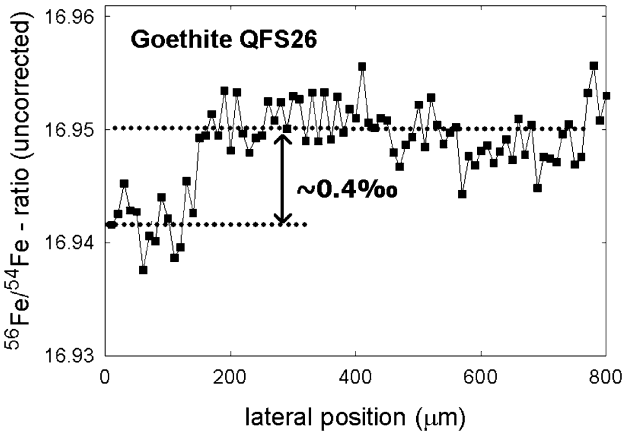

Fig. 8. Line-scan across the goethite grain QFS 26 showing an abrupt change in the ^{56}Fe/^{54}Fe ratio. The lateral position corresponds to the cycle data (2 s) at a scan speed of 5 μm/s. These changes in ^{56}Fe/^{54}Fe reflect real sample heterogeneities in δ^{56}Fe. This type of heterogeneities can easily be overlooked when using bulk-sampling techniques.

−0.52‰ (LA), which compares well to the average value of −0.51 ± 0.07‰ determined by solution ICP. The four determinations carried out by solution ICP range from −0.48 to −0.56‰ while the laser analysis (20 raster and 2 spots) show a higher variation ranging from −0.40 to −0.75‰ (Fig. 2F). As shown in Figs. 7 and 8, the goethite shows a larger heterogeneity than the high-temperature minerals and not as clear an evolution as the fibrous hematite. The scan on Fig. 8 shows a clear difference of ~0.4‰. Most of the analyses cluster around a value of −0.48 ± 0.10‰ (17 analyses) similar to the heaviest value determined in solution (Fig. 2F).

4. Discussion of hydrothermal ore-forming processes

As mentioned above, the Schwarzwald iron mineralisations record at least two major events (Markl et al., 2006). Bulk minerals separated from a variety of mines distributed over an area of 50 × 60 km were analysed by solution ICP (Markl et al., 2006). Primary hematites gave a range in δ^{56}Fe of −0.7 to +0.7‰, primary siderite gave a range of −1.4 to −0.7‰, secondary, fibrous hematite ("Glaskopf") gave a range of −1.5 to −0.4‰, and secondary goethite gave a range of −1.1 to −0.4‰. The intra-mineral isotope range found by our new in situ data encompass or even exceed this entire range within one single crystal: primary siderites M420 and OCR468 (Figs. 2D and 5) are zoned from −1.8‰ in the core to −0.5‰ at the rim. The secondary hematites Fe13 and PHB-4 show exactly the reverse pattern with −0.6‰ in the core to −1.85‰ in the rim (Figs. 2 and 6). Secondary goethite QFS26 ranges from −0.4 (core) to −0.7‰ (rim) (Fig. 2F), which is, again, similar to the bulk mineral range. In view of the findings by Markl et al. (2006) and in light of published fractionation factors, we explain these phenomena as follows.

Precipitation of siderite from a Fe(II)-bearing solution at a temperature of 150 °C was determined by spectroscopic

data (Polyakov and Mineev, 2000) to be −1.35‰ lighter than the Fe(II)-hexa-aqua-complex (when calculating the values based on the β-factors (reduced isotopic partition function ratio) for siderite (Polyakov and Mineev, 2000) and those determined for the hexa-aqua-complex by DFT PCM—Density Functional Theory—polarized continuum model, Anbar et al. (2005)), while experimental investigations at room temperature resulted in a $\Delta^{56}Fe_{siderite} - Fe^{(II)}_{aq}$ of −0.48‰ (Wiesli et al., 2004; $\Delta_{Product-Reactand}$ refers to the isotope fractionation of $^{56}Fe/^{54}Fe$ between the reactand Fe^{II}_{aq} and the product (siderite)). Caution is required when comparing β-values of Polyakov and Mineev (2000) for mineral phases with those of Anbar et al. (2005) and Schauble et al. (2001) for the hexa-aqua-complex, which may lead to systematic errors of which the magnitude is unknown. However, the measured siderite δ^{56}Fe values are in general agreement with these predictions and point towards a fluid composition around 0 to −0.5‰. The general increase of the δ^{56}Fe values towards the rim can be attributed to the precipitation of siderite along the downstream fluid pathway, removing isotopically light Fe from the fluid and, therefore, shifting its residual composition towards heavier values in a Rayleigh-type process. The fluid composition may hence have changed from about −0.3‰ to +0.9‰ in the course of the formation of the analysed siderite M420. The drop in δ^{56}Fe along the fracture of the grain (OCR486, Fig. 5) seems to be due to later infiltration by a different fluid containing light, unfractionated Fe.

The zoned hematites show the reverse isotope pattern which is challenging to explain. However, three potential explanations can be envisioned. We will discuss these in some detail.

4.1. Rayleigh-style enrichment of light isotopes during fluid oxidation

Under equilibrium conditions, the controlling reaction would be the oxidation process of an $Fe(II)(H_2O)_6$-bearing to an $Fe(III)(H_2O)_6$-bearing fluid. Using the fractionation factors published by Anbar et al. (2005) the Fe(III) would be enriched in heavy Fe by +0.75‰ at 250 °C. Given the low solubility of $Fe(III)_{aq}$, complete removal into hematite can be assumed. Assuming that no further fractionation has taken place during the crystallisation of hematite from $Fe(III)(H_2O)_6$ as it was proposed for slow hematite formation by Skulan et al. (2002), the hematite would preserve these more positive values. The residual $Fe(II)_{aq}$ would then evolve towards lighter compositions. This scenario would produce hematite along the fluid pathway with an isotopic signature that would show a heavier ratio in the core and lighter values at the rim. This is indeed observed (Fig. 6). However, in order to achieve δ^{56}Fe values as low as −1.5‰ (hematite), the fluid composition needs to be unrealistically light with values of −2.2 to −2.6‰ when using the fractionation factor determined by Anbar et al., 2005 for temperatures between 200 and 300 °C. Therefore, we regard this scenario as unlikely.

4.2. Kinetic isotope fractionation during hematite crystallisation

Kinetic isotope fractionation reported for the precipitation of hematite from $Fe(III)_{aq}$ would incorporate Fe that is lighter by up to 1‰, depending on the precipitation rate (Skulan et al., 2002). However, under static precipitation rates this would produce a zonation of the hematite that is opposite to the observed pattern. A change in the growth rate accompanied by an increase in the kinetic fractionation towards lighter values due to the continuous increase in surface area would incorporate lighter Fe towards the rim of the hematites, and would produce the observed growth banding in the hematite if the change in the fluid composition is slightly slower than the change in the kinetic fractionation. However, this shift to light hematite would be superimposed onto the fractionation of +0.75‰ (150 °C) from the oxidation of the original $Fe(II)_{aq}$. Therefore, while this scenario might just be possible for the core compositions, it is unclear how Fe as light as −1.8‰ would be incorporated into the rim. This would require an exceedingly light fluid or an extremely large kinetic fractionation factor of −2.5‰. Furthermore, in a closed system, the fluid would be continuously depleted in light Fe and would hence evolve towards heavier compositions. Because the hematites are zoned towards lighter compositions, and from the geological point of view the fluid composition should be close to 0‰ (Markl et al., 2006), we also regard this scenario as unlikely.

4.3. Dissolution of zoned siderite

The observed signature can be explained by the dissolution of siderite and quantitative redeposition as hematite under oxidizing conditions. CO_2-undersaturated meteoric water in disequilibrium with siderite would be able to dissolve the primary siderite; quantitative oxidation of Fe would precipitate Fe-oxyhydroxides, which may be transported only over a short distance (cm to tens of meters) in suspension before final precipitation. During quantitative redeposition, no fractionation will occur so that the hematite would fully represent the isotopic signature of the secondary fluid which is the composition of the primary siderite. Siderite M420 has a value of −1.8‰ in the core while the rim has a δ^{56}Fe of −0.6‰; hematite PHB-4 has a composition of −0.6 in the core and −1.8 at the rim. The observed pattern in hematite PHB-4 can, therefore, be produced by sequential layer by layer dissolution of one or a few single crystals of siderite and quantitative and near-field redeposition of the Fe as hematite. The dominance of Mn relative to other trace elements in the hematite also points towards siderite as a potential source of Fe. This case illustrates that mineral deposits are remobilised with time and that the hematite just represents a secondary remobilisation of Fe maintaining the initial isotopic signature of the fluid.

5. Conclusions

It has been demonstrated that UV-femtosecond laser ablation provides a tool for in situ, high spatial resolution MC-ICP-MS, stable isotope ratio measurements of Fe. A matrix dependency of samples when calibrated against a pure metal isotopic standard such as IRMM-14 was not observed. This was shown for Fe meteorites, Fe oxides (hematite and magnetite), Fe carbonate (siderite), and Fe-hydroxide (goethite). New data on Fe-sulphides (Horn et al. unpublished) also follows this rule (Fig. 9). Mass bias artefacts that exceed the precision of the measurements as reported by Jackson and Guenther (2003) and Kosler et al. (2005), were absent. Furthermore, there was always good agreement between the results obtained for single spot analyses and those obtained from raster analysis. A reproducibility in δ^{56}Fe of ~0.1‰ (2 sigma) was obtained on homogeneous minerals. By comparison to solution Fe-isotope analysis a general accuracy in the δ^{56}Fe values of better than 0.1‰ can be achieved for fs-UV laser ablation measurements. However, most minerals analysed show an internal isotopic heterogeneity that exceeds the external reproducibility allowing zonations and growth sequences to become "visible". This shows that bulk sampling and dissolution techniques can only provide us with an average isotopic composition and that much of the information recorded by a single mineral grain is lost. Micro-sampling with laser ablation provides us with a spatial resolution that adds a further dimension to our interpretation of stable metal isotope fractionation.

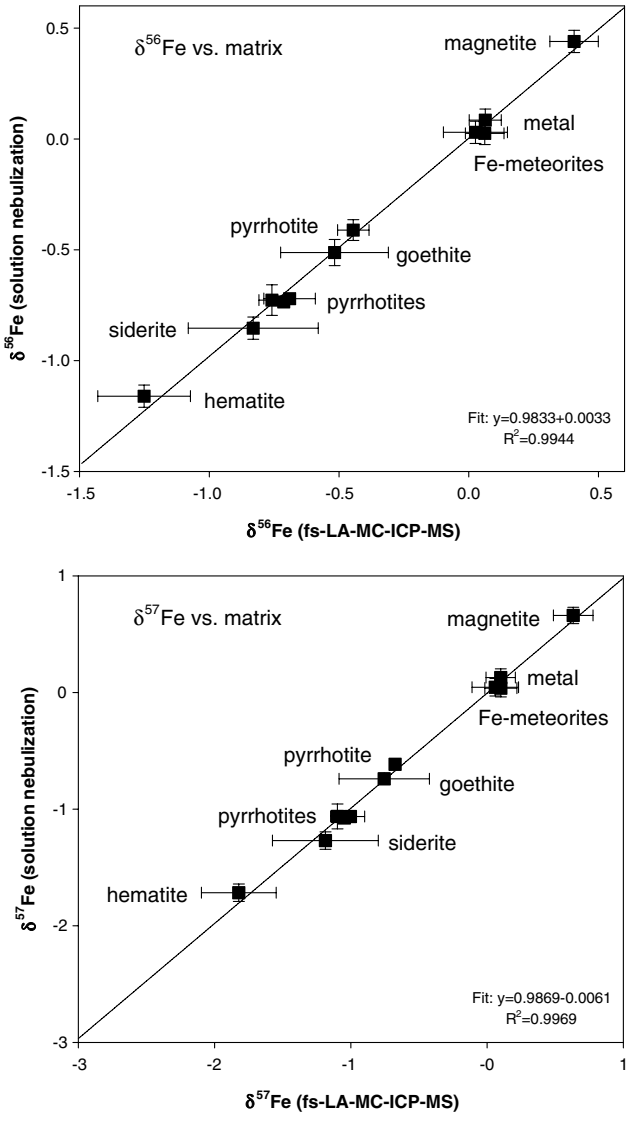

Fig. 9. Comparison between the δ^{56}Fe and ^{57}Fe values obtained conventionally by solution ICP-MS with those obtained in situ by fs-LA-MC-ICP-MS. The matrix-independent calibration has been further validated with analysis of pyrrhotite (Horn, unpublished) illustrating that oxides, hydroxides, carbonates, metals, and sulphides can be determined at high precision without loss in accuracy. In some samples the large error bars of the LA data correspond to sample heterogeneity.

The complexity of the isotopic evolution within a hydrothermal mineral deposit becomes obvious when comparing the isotopic variations found in single mineral grains. In some cases, these exceed 1.5‰ over a distance of 2 cm, which is a substantial fraction of the variation found so far in natural materials throughout the Earth's history (~4‰). The variations found in the hydrothermal mineralisations from the Schwarzwald area can be explained by primary siderite precipitation from carbonate-rich fluids. The preferential incorporation of light Fe into the siderite results in a Rayleigh-type fluid evolution towards heavier compositions. This is traced by the siderite itself, which contains light Fe in the core and heavy Fe in the rim. Later, dissolution of the zoned siderite, involving a second low-temperature oxidation event, completely deposited the siderite-derived Fe as hematite under oxidising conditions. This results in a reversed isotopic pattern with heavy Fe in the core and lighter Fe at the rim of hematites. The microanalysis of ore mineral isotope compositions, therefore, provides insights into fluid evolution histories, and allows for the tracing of breakdown products that are transported, through an oxidising fluid, into second-generation mineralisations.

Acknowledgments

We acknowledge the support for this study by the German Science Foundation (DFG) Grant HO 3257/1 and the Volkswagenstiftung. W. Hurkuck, B. Aichinger, and O. Dietrich are thanked for technical support. We are grateful to A. Anbar and S. Weyer for their constructive reviews, and M. Rehkämper for efficient editorial handling.

Associate editor: Mark Rehkamper

References

Anbar, A.D., 2004. Iron stable isotopes: beyond biosignatures. *Earth Planet. Sci. Lett.* **217**, 223–236.

Anbar, A.D., Jarzecki, A.A., Spiro, T.G., 2005. Theoretical investigation of iron isotope fractionation between $Fe(H_2O)_6^{3+}$ and $Fe(H_2O)_6^{2+}$: implications for iron stable isotope geochemistry. *Geochim. Cosmochim. Acta* **69**, 825–837.

Beard, B.L., Johnson, C.M., 2004a. Fe isotope variations in the modern and ancient earth and other planetary bodies. In: Johnson, C.M., Beard, B.L., Albarede, F. (Eds.), *Geochemistry of Non-Traditional Stable Isotopes*, *Reviews in Mineralogy and Geochemistry*, 55. Mineralogical Society of America, Blacksburg, pp. 319–357.

Beard, B.L., Johnson, C.M., 2004b. Inter-mineral Fe isotope variations in mantle-derived rocks and implications for the Fe geochemical cycle. *Geochim. Cosmochim. Acta* **68**, 4727–4743.

Belshaw, N.S., Zhu, X.K., Guo, Y., O'Nions, R.K., 2000. High precision measurement of iron isotopes by plasma source mass spectrometry. *Int. J. Mass Spectrom.* **197**, 191–195.

Brantley, S.L., Liermann, L.J., Guynn, R.L., Anbar, A., Icopini, G.A., Barling, J., 2004. Fe isotopic fractionation during mineral dissolution with and without bacteria. *Geochim. Cosmochim. Acta* **68**, 3189–3204.

Brockamp, O., Clauer, N., 2005. A km-scale illite alteration zone in sedimentary wall rocks adjacent to a hydrothermal fluorite vein deposit. *Clay Min.* **40**, 245–260.

Butler, I.B., Archer, C., Vance, D., Oldroyd, A., Rickard, D., 2005. Fe isotope fractionation on FeS formation in ambient aqueous solution. *Earth Planet. Sci. Lett.* **236**, 430–442.

Choi, B.G., Ouyang, X.W., Wasson, J.T., 1995. Classification and origin of IAB and IIICD iron meteorites. *Geochim. Cosmochim. Acta* **59**, 593–612.

Croal, L.R., Johnson, C.M., Beard, B.L., Newman, D.K., 2004. Iron isotope fractionation by Fe(II)-oxidizing photoautotrophic bacteria. *Geochim. Cosmochim. Acta* **68**, 1227–1242.

Dauphas, N., Rouxel, O., 2006. Mass Spectrometry and natural variations of iron isotopes. *Mass Spectrom. Rev.* **25**, 515–550.

Dauphas, N., van Zuilen, M., Wadhwa, M., Davis, A.M., Marty, B., Janney, P.E., 2004. Clues from Fe isotope variations on the origin of early Archean BIFs from Greenland. *Science* **306**, 2077–2080.

Eggins, S.M., 2003. Laser ablation ICP-MS analysis of geological materials prepared as lithium borate glasses. *Geostand. Newslett.* **27**, 147–162.

Fantle, M.S., De Paolo, D.J., 2004. Iron isotopic fractionation during continental weathering. *Earth Planet. Sci. Lett.* **228**, 547–562.

Frost, C.D., von Blanckenburg, F., Schoenberg, R., Frost, B.R., Swapp, S.M., 2005. Preservation of Fe isotope compositions of iron formation during contact metamorphism. *Geochim. Cosmochim. Acta* **69**, A218.

Graham, S., Pearson, N., Jackson, S., Griffin, W., O'Reilly, S.Y., 2004. Tracing Cu and Fe from source to porphyry: in situ determination of Cu and Fe isotope ratios in sulfides from the Grasberg Cu-Au deposit. *Chem. Geol.* **207**, 147–169.

Günther, D., Audetat, A., Frischknecht, R., Heinrich, C.A., 1998. Quantitative analysis of major, minor and trace elements in fluid inclusions using laser ablation inductively coupled plasma mass spectrometry. *J. Anal. At. Spectrom.* **13**, 263–270.

Günther, D., Bleiner, D., Guillong, M., Hattendorf, B., Horn, I., 2001. Access to isotopic and elemental composition and their distribution in solid materials by laser ablation-inductively coupled plasma-mass spectrometry. *Chimia* **55**, 778–782.

Halpin, J.A., Gerakiteys, C.L., Clarke, G.L., Belousova, E.A., Griffin, W.L., 2005. In-situ U-Pb geochronology and Hf isotope analyses of the Rayner Complex, East Antarctica. *Contrib. Miner. Petrol.* **148**, 689–706.

Horn, I., Hinton, R.W., Jackson, S.E., Longerich, H.P., 1997. Ultra-trace element analysis of NIST SRM 616 and 614 using laser ablation microprobe inductively coupled plasma mass spectrometry (LAM-ICP-MS): a comparison with secondary ion mass spectrometry (SIMS). *Geostand. Newslett.* **21**, 191–203.

Horn, I., Rudnick, R.L., Mcdonough, W.F., 2000. Precise elemental and isotope ratio determination by simultaneous solution nebulization and laser ablation-ICP-MS: application to U-Pb geochronology. *Chem. Geol.* **167**, 405–425.

Horn, I., Schoenberg, R., von Blanckenburg, F., 2006. Comment on "Analysis of Fe isotopes in sulfides and iron meteorites by laser ablation high-mass resolution multi-collector ICP mass spectrometry". In: Kosler, J., Pedersen, R.B., Kruber, C., Sylvester, P.J. (Eds.). *J. Anal. At. Spectrom.* **21**, 211–213.

Icopini, G.A., Anbar, A.D., Ruebush, S.S., Tien, M., Brantley, S.L., 2004. Iron isotope fractionation during microbial reduction of iron: the importance of adsorption. *Geology* **32**, 205–208.

Jackson, S.E., Guenther, D., 2003. The nature and sources of laser induced isotopic fractionation in laser ablation-multicollector-inductively coupled plasma-mass spectrometry. *J. Anal. At. Spectrom.* **18**, 205–212.

Johnson, C.M., Beard, B.L., Roden, E.E., Newman, D.K., Nealson, K.H., 2004. Isotopic constraints on biogeochemical cycling of Fe. In: Johnson, C.M., Beard, B.L., Albarede, F. (Eds.), *Geochemistry of Non-Traditional Stable Isotopes*, *Reviews in Mineralogy and Geochemistry*, vol. 55. Mineralogical Society of America, Blacksburg, pp. 359–408.

Johnson, C.M., Roden, E.E., Welch, S.A., Beard, B.L., 2005. Experimental constraints on Fe isotope fractionation during magnetite and Fe carbonate formation coupled to dissimilatory hydrous ferric oxide reduction. *Geochim. Cosmochim. Acta* **69**, 963–993.

Kehm, K., Hauri, E.H., Alexander, C.M.O., Carlson, R.W., 2003. High precision iron isotope measurements of meteoritic material by cold plasma ICP-MS. *Geochim. Cosmochim. Acta* **67**, 2879–2891.

Kosler, J., Pedersen, R.B., Kruber, C., Sylvester, P.J., 2005. Analysis of Fe isotopes in sulfides and iron meteorites by laser ablation high-mass resolution multi-collector ICP mass spectrometry. *J. Anal. At. Spectrom.* **20**, 192–199.

Ludwig, K. R., 2001. ISOPLOT: a plotting and regression program for radiogenic isotope data, version 2.49. Berkeley, *Geochron. Cent. Spec. Publ. 1a.*

Markl, G., von Blanckenburg, F., Wagner, T., 2006. Iron isotope fractionation during hydrothermal ore deposition and alterration. *Geochim. Cosmochim. Acta.* **70**, 3011–3030.

Mason, P.R.D., Mank, A.J.G., 2001. Depth-resolved analysis in multi-layered glass and metal materials using laser ablation inductively coupled plasma mass spectrometry (LA-ICP-MS). *J. Anal. At. Spectrom.* **16**, 1381–1388.

Matthews, A., Morgans-Bell, H.S., Emmanuel, S., Jenkyns, H.C., Erel, Y., Halicz, L., 2004. Controls on iron-isotope fractionation in organic-rich sediments (Kimmeridge Clay, Upper Jurassic, southern England). *Geochim. Cosmochim. Acta* **68**, 3107–3123.

Matthews, A., Zhu, X.K., O'Nions, K., 2001. Kinetic iron stable isotope fractionation between iron (-II) and (-III) complexes in solution. *Earth Planet. Sci. Lett.* **192**, 81–92.

Poitrasson, F., Halliday, A.N., Lee, D.C., Levasseur, S., Teutsch, N., 2004. Iron isotope differences between Earth, Moon, Mars and Vesta as possible records of contrasted accretion mechanisms. *Earth Planet. Sci. Lett.* **223**, 253–266.

Poitrasson, F., Levasseur, S., Teutsch, N., 2005. Significance of iron isotope mineral fractionation in pallasites and iron meteorites for the core-mantle differentiation of terrestrial planets. *Earth Planet. Sci. Lett.* **234**, 151–164.

Poitrasson, F., Mao, X.L., Mao, S.S., Freydier, R., Russo, R.E., 2003. Comparison of ultraviolet femtosecond and nanosecond laser ablation inductively coupled plasma mass spectrometry analysis in glass, monazite, and zircon. *Anal. Chem.* **75**, 6184–6190.

Polyakov, V.B., Mineev, S.D., 2000. The use of Mossbauer spectroscopy in stable isotope geochemistry. *Geochim. Cosmochim. Acta* **64**, 849–865.

Poulson, R.L., Johnson, C.M., Beard, B.L., 2005. Iron isotope exchange kinetics at the nanoparticulate ferrihydrite surface. *Am. Mineral.* **90**, 758–763.

Ramos, F.C., Wolff, J.A., Tollstrup, D.L., 2004. Measuring Sr-87/Sr-86 variations in minerals and groundmass from basalts using LA-MC-ICPMS. *Chem. Geol.* **211**, 135–158.

Rasmussen, K.L., Malvin, D.J., Buchwald, V.F., Wasson, J.T., 1984. Compositional trends and cooling rates of group IVB iron-meteorites. *Geochim. Cosmochim. Acta* **48**, 805–813.

Rasmussen, K.L., Malvin, D.J., Wasson, J.T., 1988. Trace-element partitioning between taenite and kamacite—relationship to the cooling rates of iron-meteorites. *Meteoritics* **23**, 107–112.

Rouxel, O., Fouquet, Y., Ludden, J.N., 2004. Subsurface processes at the Lucky Strike hydrothermal field, Mid-Atlantic Ridge: evidence from sulfur, selenium, and iron isotopes. *Geochim. Cosmochim. Acta* **68**, 2295–2311.

Rouxel, O.J., Bekker, A., Edwards, K.J., 2005. Iron isotope constraints on the Archean and Paleoproterozoic ocean redox state. *Science* **307**, 1088–1091.

Russo, R.E., Mao, X.L., Liu, H.C., Gonzalez, J., Mao, S.S., 2002. Laser ablation in analytical chemistry—a review. *Talanta* **57**, 425–451.

Schauble, E.A., 2004. Applying stable isotope fractionation theory to new systems. In: Johnson, C.M., Beard, B.L., Albarede, F. (Eds.), *Geochemistry of Non-Traditional Stable Isotopes*, *Reviews in Mineralogy and Geochemistry*, 55. Mineralogical Society of America, Blacksburg, pp. 65–111.

Schauble, E.A., Rossman, G.R., Taylor, H.P., 2001. Theoretical estimates of equilibrium Fe-isotope fractionations from vibrational spectroscopy. *Geochim. Cosmochim. Acta* **65**, 2487–2497.

Schoenberg, R., von Blanckenburg, F., 2005. An assessment of the accuracy of stable Fe isotope ratio measurements on samples with organic and inorganic matrices by high-resolution multicollector ICP-MS. *Int. J. Mass spectrom.* **242**, 257–272.

Schwinn, G., Markl, G., 2005. REE systematics in hydrothermal fluorite. *Chem. Geol.* **216**, 225–248.

Schwinn, G., Wagner, T., Baldorj, B., Markl, G., 2006. Quantification of mixing processes in ore-forming hydrothermal systems by combination of stable isotope and fluid inclusion analyses. *Geochim. Cosmochim. Acta.* **70**, 965–982.

Severmann, S., Johnson, C.M., Beard, B.L., German, C.R., Edmonds, H.N., Chiba, H., Green, D.R.H., 2004. The effect of plume processes on the Fe isotope composition of hydrothermally derived Fe in the deep ocean as inferred from the Rainbow vent site, Mid-Atlantic Ridge, 36 degrees 14′ N. *Earth Planet. Sci. Lett.* **225**, 63–76.

Skulan, J.L., Beard, B.L., Johnson, C.M., 2002. Kinetic and equilibrium Fe isotope fractionation between aqueous Fe(III) and hematite. *Geochim. Cosmochim. Acta* **66**, 2995–3015.

Thirlwall, M.F., Walder, A.J., 1995. In situ hafnium isotope ratio analysis of zircon by inductively coupled plasma multiple collector mass spectrometry. *Chem. Geol.* **122**, 241–247.

Walczyk, T., von Blanckenburg, F., 2005. Deciphering the iron isotope message of the human body. *Int. J. Mass spectrom.* **242**, 117–134.

Welch, S.A., Beard, B.L., Johnson, C.M., Braterman, P.S., 2003. Kinetic and equilibrium Fe isotope fractionation between aqueous Fe(II) and Fe(III). *Geochim. Cosmochim. Acta* **67**, 4231–4250.

Weyer, S., Anbar, A.D., Brey, G.P., Munker, C., Mezger, K., Woodland, A.B., 2005. Iron isotope fractionation during planetary differentiation. *Earth Planet. Sci. Lett.* **240**, 251–264.

Weyer, S., Schwieters, J., 2003. High precision Fe isotope measurements with high mass resolution MC-ICPMS. *Int. J. Mass spectrom.* **226**, 355–368.

Wiesli, R.A., Beard, B.L., Johnson, C.M., 2004. Experimental determination of Fe isotope fractionation between aqueous Fe(II), siderite and "green rust" in abiotic systems. *Chem. Geol.* **211**, 343–362.

Williams, H.M., McCammon, C.A., Peslier, A.H., Halliday, A.N., Teutsch, N., Levasseur, S., Burg, J.P., 2004. Iron isotope fractionation and the oxygen fugacity of the mantle. *Science* **304**, 1656–1659.

Woodhead, J., Hergt, J., Shelley, M., Eggins, S., Kemp, R., 2004. Zircon Hf-isotope analysis with an excimer laser, depth profiling, ablation of complex geometries, and concomitant age estimation. *Chem. Geol.* **209**, 121–135.

Woodhead, J., Swearer, S., Hergta, J., Maasa, R., 2005. In situ Sr-isotope analysis of carbonates by LA-MC-ICP-MS: interference corrections, high spatial resolution and an example from otolith studies. *J. Anal. At. Spectrom.* **20**, 22–27.

Young, E.D., Ash, R.D., Galy, A., Belshaw, N.S., 2002. Mg isotope heterogeneity in the Allende meteorite measured by UV laser ablation-MC-ICPMS and comparisons with O isotopes. *Geochim. Cosmochim. Acta* **66**, 683–698.

Zhu, X.K., Guo, Y., O'Nions, R.K., Young, E.D., Ash, R.D., 2001. Isotopic homogeneity of iron in the early solar nebula. *Nature* **412**, 311–313.

Zhu, X.K., Guo, Y., Williams, R.J.P., O'Nions, R.K., Matthews, A., Belshaw, N.S., Canters, G.W., de Waal, E.C., Weser, U., Burgess, B.K., Salvato, B., 2002. Mass fractionation processes of transition metal isotopes. *Earth Planet. Sci. Lett.* **200**, 47–62.